cardiac action potentials in freely beating rabbit hearts, pp. 3578–3580, 2004, with permission from IEEE.

References

Aimond, F., Alvarez, J.L., Rauzier, J.M., Lorente, P., Vassort, G., 1999. Ionic basis of ventricular arrhythmias in remodeled rat heart during long-term myocardial infarction. Cardiovasc. Res. 42, 402–415.

Allen, D.G., Kentish, J.C., 1988. Calcium concentration in the myoplasm of skinned ferret ventricular muscle following changes in muscle length. J. Physiol. 407, 489–503.

Bagwe, S., Berenfeld, O., Vaidya, D., Morley, G.E., Jalife, J., 2005. Altered right atrial excitation and propagation in connexin40 knockout mice. Circulation 112, 2245–2253.

Belus, A., White, E., 2003. Streptomycin and intracellular calcium modulate the response of single guinea-pig ventricular myocytes to axial stretch. J. Physiol. 546, 501–509.

Bett, G.C., Sachs, F., 2000. Whole-cell mechanosensitive currents in rat ventricular myocytes activated by direct stimulation. J. Membr. Biol. 173, 255–263.

Bourgeois, E.B., Bachtel, A.D., Huang, J., Walcott, G.P., Rogers, J.M., 2011. Simultaneous optical mapping of transmembrane potential and wall motion in isolated, perfused whole hearts. J. Biomed. Opt. 16, 096020.

Bourgeois, E.B., Reeves, H.D., Walcott, G.P., Rogers, J.M., 2012. Panoramic optical mapping shows wavebreak at a consistent anatomical site at the onset of ventricular fibrillation. Cardiovasc. Res. 93, 272–279.

Bullen, A., Saggau, P., 1999. High-speed, random-access fluorescence microscopy: II. Fast quantitative measurements with voltage-sensitive dyes. Biophys. J. 76, 2272–2287.

Calaghan, S., White, E., 2004. Activation of Na+-H+ exchange and stretch-activated channels underlies the slow inotropic response to stretch in myocytes and muscle from the rat heart. J. Physiol. 559, 205–214.

Chen, R.L., Penny, D.J., Greve, G., Lab, M.J., 2004. Stretch-induced regional mechanoelectric dispersion and arrhythmia in the right ventricle of anesthetized lambs. Am. J. Physiol. Heart Circ. Physiol. 286, H1008–H1014.

Craelius, W., Chen, V., el-Sherif, N., 1988. Stretch activated ion channels in ventricular myocytes. Biosci. Rep. 8, 407–414.

Efimov, I., Salama, G., 2012. The future of optical mapping is bright: RE: review on: "Optical Imaging of Voltage and Calcium in Cardiac Cells and Tissues" by Herron, Lee, and Jalife. Circ. Res. 110, e70-1.

Efimov, I.R., Nikolski, V.P., Salama, G., 2004. Optical imaging of the heart. Circ. Res. 95, 21–33.

Fasciano 2nd, R.W., Tung, L., 1999. Factors governing mechanical stimulation in frog hearts. Am. J. Physiol. 277, H2311–H2320.

Fluhler, E., Burnham, V.G., Loew, L.M., 1985. Spectra, membrane binding, and potentiometric responses of new charge shift probes. Biochemistry 24, 5749–5755.

Franz, M.R., Burkhoff, D., Yue, D.T., Sagawa, K., 1989. Mechanically induced action potential changes and arrhythmia in isolated and in situ canine hearts. Cardiovasc Res. 23, 213–223.

Franz, M.R., Cima, R., Wang, D., Profitt, D., Kurz, R., 1992. Electrophysiological effects of myocardial stretch and mechanical determinants of stretch-activated arrhythmias. Circulation 86, 968–978.

Fujiwara, K., Tanaka, H., Mani, H., Nakagami, T., Takamatsu, T., 2008. Burst emergence of intracellular Ca2+ waves evokes arrhythmogenic oscillatory depolarization via the Na+-Ca2+ exchanger: simultaneous confocal recording of membrane potential and intracellular Ca2+ in the heart. Circ. Res. 103, 509–518.

Gannier, F., White, E., Lacampagne, A., Garnier, D., Le Guennec, J.Y., 1994. Streptomycin reverses a large stretch induced increases in [Ca2+]i in isolated guinea pig ventricular myocytes. Cardiovasc. Res. 28, 1193–1198.

Garnier, D., 1994. Attachment procedures for mechanical manipulation of isolated cardiac myocytes: a challenge. Cardiovasc. Res. 28, 1758–1764.

Garny, A., Kohl, P., 2004. Mechanical induction of arrhythmias during ventricular repolarization: modeling cellular mechanisms and their interaction in two dimensions. Ann. N. Y. Acad. Sci. 1015, 133–143.

Hansen, D.E., Borganelli, M., Stacy Jr., G.P., Taylor, L.K., 1991. Dose-dependent inhibition of stretch-induced arrhythmias by gadolinium in isolated canine ventricles. Evidence for a unique mode of antiarrhythmic action. Circ. Res. 69, 820–831.

Hansen, D.E., Craig, C.S., Hondeghem, L.M., 1990. Stretch-induced arrhythmias in the isolated canine ventricle. Evidence for the importance of mechanoelectrical feedback. Circulation 81, 1094–1105.

Herron, T.J., Lee, P., Jalife, J., 2012. Optical imaging of voltage and calcium in cardiac cells & tissues. Circ. Res. 110, 609–623.

Inagaki, M., Hidaka, I., Aiba, T., Tatewaki, T., Sunagawa, K., Sugimachi, M., 2004. High resolution optical mapping of cardiac action potentials in freely beating rabbit hearts. Conf. Proc. IEEE Eng. Med. Biol. Soc. 5, 3578–3580.

Iribe, G., Helmes, M., Kohl, P., 2007. Force-length relations in isolated intact cardiomyocytes subjected to dynamic changes in mechanical load. Am. J. Physiol. Heart Circ. Physiol. 292, H1487–H1497.

Iribe, G., Jin, H., Kaihara, K., Naruse, K., 2010. Effects of axial stretch on sarcolemmal BKCa channels in post-hatch chick ventricular myocytes. Exp. Physiol. 95, 699–711.

Iribe, G., Ward, C.W., Camelliti, P., Bollensdorff, C., Mason, F., Burton, R.A., Garny, A., Morphew, M.K., Hoenger, A., Lederer, W.J., Kohl, P., 2009. Axial stretch of rat single ventricular cardiomyocytes causes an acute and transient increase in Ca2+ spark rate. Circ. Res. 104, 787–795.

Janse, M.J., 2004. Electrophysiological changes in heart failure and their relationship to arrhythmogenesis. Cardiovasc. Res. 61, 208–217.

Jian, Z., Han, H., Zhang, T., Puglisi, J., Izu, L.T., Shaw, J.A., Onofiok, E., Erickson, J.R., Chen, Y.J., Horvath, B., Shimkunas, R., Xiao, W., Li, Y., Pan, T., Chan, J., Banyasz, T., Tardiff, J.C., Chiamvimonvat, N., Bers, D.M., Lam, K.S., Chen-Izu, Y., 2014. Mechanochemotransduction during cardiomyocyte contraction is mediated by localized nitric oxide signaling. Sci. Signal 7, ra27.

Kamkin, A., Kiseleva, I., Isenberg, G., 2000. Stretch-activated currents in ventricular myocytes: amplitude and arrhythmogenic effects increase with hypertrophy. Cardiovasc. Res. 48, 409–420.

Kamkin, A., Kiseleva, I., Isenberg, G., 2003. Ion selectivity of stretch-activated cation currents in mouse ventricular myocytes. Pflugers Arch. 446, 220–231.

Katz, A.M., Katz, P.B., 1989. Homogeneity out of heterogeneity. Circulation 79, 712–717.

Kay, M.W., Walcott, G.P., Gladden, J.D., Melnick, S.B., Rogers, J.M., 2006. Lifetimes of epicardial rotors in panoramic optical maps of fibrillating swine ventricles. Am. J. Physiol. Heart Circ. Physiol. 291, H1935–H1941.

Khairallah, R.J., Shi, G., Sbrana, F., Prosser, B.L., Borroto, C., Mazaitis, M.J., Hoffman, E.P., Mahurkar, A., Sachs, F., Sun, Y., Chen, Y.W., Raiteri, R., Lederer, W.J., Dorsey, S.G., Ward, C.W., 2012. Microtubules underlie dysfunction in duchenne muscular dystrophy. Sci. Signal 5, ra56.

Knisley, S.B., Justice, R.K., Kong, W., Johnson, P.L., 2000. Ratiometry of transmembrane voltage-sensitive fluorescent dye emission in hearts. Am. J. Physiol. Heart Circ. Physiol. 279, H1421–H1433.

Kohl, P., Day, K., Noble, D., 1998. Cellular mechanisms of cardiac mechano-electric feedback in a mathematical model. Can. J. Cardiol. 14, 111–119.

Kohl, P., Sachs, F., Franz, M.R., 2011. Cardiac Mechano-electric Coupling and Arrhythmias, second ed. Oxford University Press, Oxford ; New York.

Kong, C.R., Bursac, N., Tung, L., 2005. Mechanoelectrical excitation by fluid jets in monolayers of cultured cardiac myocytes. J. Appl. Physiol. (1985) 98, 2328–2336 discussion 2320.

Le Guennec, J.Y., Peineau, N., Argibay, J.A., Mongo, K.G., Garnier, D., 1990. A new method of attachment of isolated mammalian ventricular myocytes for tension recording: length dependence of passive and active tension. J. Mol. Cell. Cardiol. 22, 1083–1093.

Lerman, B.B., Burkhoff, D., Yue, D.T., Franz, M.R., Sagawa, K., 1985. Mechanoelectrical feedback: independent role of preload and contractility in modulation of canine ventricular excitability. J. Clin. Invest. 76, 1843–1850.

Li, W., Kohl, P., Trayanova, N., 2004. Induction of ventricular arrhythmias following mechanical impact: a simulation study in 3D. J. Mol. Histol. 35, 679–686.

Link, M.S., 2012. Commotio cordis: ventricular fibrillation triggered by chest impact-induced abnormalities in repolarization. Circ. Arrhythm. Electrophysiol. 5, 425–432.

Link, M.S., Maron, B.J., Wang, P.J., VanderBrink, B.A., Zhu, W., Estes 3rd, N.A., 2003. Upper and lower limits of vulnerability to sudden arrhythmic death with chest-wall impact (commotio cordis). J. Am. Coll. Cardiol. 41, 99–104.

Lou, Q., Li, W., Efimov, I.R., 2012. The role of dynamic instability and wavelength in arrhythmia maintenance as revealed by panoramic imaging with blebbistatin vs. 2,3-butanedione monoxime. Am. J. Physiol. Heart Circ. Physiol. 302, H262–H269.

Madias, C., Maron, B.J., Supron, S., Estes 3rd, N.A., Link, M.S., 2008. Cell membrane stretch and chest blow-induced ventricular fibrillation: commotio cordis. J. Cardiovasc Electrophysiol. 19, 1304–1309.

Moore, C.C., Lugo-Olivieri, C.H., McVeigh, E.R., Zerhouni, E.A., 2000. Three-dimensional systolic strain patterns in the normal human left ventricle: characterization with tagged MR imaging. Radiology 214, 453–466.

Nishimura, S., Kawai, Y., Nakajima, T., Hosoya, Y., Fujita, H., Katoh, M., Yamashita, H., Nagai, R., Sugiura, S., 2006a. Membrane potential of rat ventricular myocytes responds to axial stretch in phase, amplitude and speed-dependent manners. Cardiovasc. Res. 72, 403–411.

Nishimura, S., Nagai, S., Katoh, M., Yamashita, H., Saeki, Y., Okada, J., Hisada, T., Nagai, R., Sugiura, S., 2006b. Microtubules modulate the stiffness of cardiomyocytes against shear stress. Circ. Res. 98, 81–87.

Nishimura, S., Seo, K., Nagasaki, M., Hosoya, Y., Yamashita, H., Fujita, H., Nagai, R., Sugiura, S., 2008. Responses of single-ventricular myocytes to dynamic axial stretching. Prog. Biophys. Mol. Biol. 97, 282–297.

Nishimura, S., Yasuda, S., Katoh, M., Yamada, K.P., Yamashita, H., Saeki, Y., Sunagawa, K., Nagai, R., Hisada, T., Sugiura, S., 2004. Single cell mechanics of rat cardiomyocytes under isometric, unloaded, and physiologically loaded conditions. Am. J. Physiol. Heart Circ. Physiol. 287, H196–H202.

Niu, W., Sachs, F., 2003. Dynamic properties of stretch-activated K+ channels in adult rat atrial myocytes. Prog. Biophys. Mol. Biol. 82, 121–135.

Palmer, R.E., Brady, A.J., Roos, K.P., 1996. Mechanical measurements from isolated cardiac myocytes using a pipette attachment system. Am. J. Physiol. 270, C697–C704.

Parker, K.K., Lavelle, J.A., Taylor, L.K., Wang, Z., Hansen, D.E., 2004. Stretch-induced ventricular arrhythmias during acute ischemia and reperfusion. J. Appl. Physiol. (1985) 97, 377–383.

Parker, K.K., Taylor, L.K., Atkinson, J.B., Hansen, D.E., Wikswo, J.P., 2001. The effects of tubulin-binding agents on stretch-induced ventricular arrhythmias. Eur. J. Pharmacol. 417, 131–140.
Pfeiffer, E.R., Tangney, J.R., Omens, J.H., McCulloch, A.D., 2014. Biomechanics of cardiac electromechanical coupling and mechanoelectric feedback. J. Biomech. Eng. 136, 021007.
Prinzen, F.W., Hunter, W.C., Wyman, B.T., McVeigh, E.R., 1999. Mapping of regional myocardial strain and work during ventricular pacing: experimental study using magnetic resonance imaging tagging. J. Am. Coll. Cardiol. 33, 1735–1742.
Prosser, B.L., Ward, C.W., Lederer, W.J., 2011. X-ROS signaling: rapid mechano-chemo transduction in heart. Science 333, 1440–1445.
Quinn, T.A., 2014. The importance of non-uniformities in mechano-electric coupling for ventricular arrhythmias. J. Interv. Card. Electrophysiol. 39, 25–35.
Quinn, T.A., Kohl, P., 2011. Mechanical triggers and facilitators of ventricular tachyarrhythmias. In: Kohl, P., Sachs, F., Franz, M.R. (Eds.), Cardiac Mechano-electric Coupling and Arrhythmais. Oxford University Press, Oxford; New York, pp. 160–167.
Ravens, U., 2003. Mechano-electric feedback and arrhythmias. Prog. Biophys. Mol. Biol. 82, 255–266.
Rice, J.J., Winslow, R.L., Dekanski, J., McVeigh, E., 1998. Model studies of the role of mechano-sensitive currents in the generation of cardiac arrhythmias. J. Theor. Biol. 190, 295–312.
Riemer, T.L., Sobie, E.A., Tung, L., 1998. Stretch-induced changes in arrhythmogenesis and excitability in experimentally based heart cell models. Am. J. Physiol. 275, H431–H442.
Riemer, T.L., Tung, L., 2003. Stretch-induced excitation and action potential changes of single cardiac cells. Prog. Biophys. Mol. Biol. 82, 97–110.
Rohde, G.K., Dawant, B.M., Lin, S.F., 2005. Correction of motion artifact in cardiac optical mapping using image registration. IEEE Trans. Biomed. Eng. 52, 338–341.
Rohr, S., Kucera, J.P., 1998. Optical recording system based on a fiber optic image conduit: assessment of microscopic activation patterns in cardiac tissue. Biophys. J. 75, 1062–1075.
Sachs, F., 2010. Stretch-activated ion channels: what are they? Physiology (Bethesda) 25, 50–56.
Sachs, F., 2011. Stretch-activated channels in the heart. In: Kohl, P., Sachs, F., Franz, M.R. (Eds.), Cardiac Mechano-electric Coupling and Arrhythmias. Oxford University Press, Oxford ; New York, pp. 11–18.
Sahakian, A.V., Peterson, M.S., Shkurovich, S., Hamer, M., Votapka, T., Ji, T., Swiryn, S., 2001. A simultaneous multichannel monophasic action potential electrode array for in vivo epicardial repolarization mapping. IEEE Trans. Biomed. Eng. 48, 345–353.
Sasaki, N., Mitsuiye, T., Noma, A., 1992. Effects of mechanical stretch on membrane currents of single ventricular myocytes of guinea-pig heart. Jpn. J. Physiol. 42, 957–970.
Schaffer, P., Ahammer, H., Muller, W., Koidl, B., Windisch, H., 1994. Di-4-ANEPPS causes photodynamic damage to isolated cardiomyocytes. Pflugers Arch. 426, 548–551.
Schuessler, R.B., Kawamoto, T., Hand, D.E., Mitsuno, M., Bromberg, B.I., Cox, J.L., Boineau, J.P., 1993. Simultaneous epicardial and endocardial activation sequence mapping in the isolated canine right atrium. Circulation 88, 250–263.
Scimia, M.C., Hurtado, C., Ray, S., Metzler, S., Wei, K., Wang, J., Woods, C.E., Purcell, N.H., Catalucci, D., Akasaka, T., Bueno, O.F., Vlasuk, G.P., Kaliman, P., Bodmer, R., Smith, L.H., Ashley, E., Mercola, M., Brown, J.H., Ruiz-Lozano, P., 2012. APJ acts as a dual receptor in cardiac hypertrophy. Nature 488, 394–398.
Seo, K., Inagaki, M., Nishimura, S., Hidaka, I., Sugimachi, M., Hisada, T., Sugiura, S., 2010. Structural heterogeneity in the ventricular wall plays a significant role in the initiation of stretch-induced arrhythmias in perfused rabbit right ventricular tissues and whole heart preparations. Circ. Res. 106, 176–184.
Seo, K., Rainer, P.P., Lee, D.I., Hao, S., Bedja, D., Birnbaumer, L., Cingolani, O.H., Kass, D.A., 2014. Hyperactive adverse mechanical stress responses in dystrophic heart are coupled to transient receptor potential canonical 6 and blocked by cGMP-protein kinase G modulation. Circ. Res. 114, 823–832.
Sugiura, S., Kobayakawa, N., Fujita, H., Yamashita, H., Momomura, S., Chaen, S., Omata, M., Sugi, H., 1998. Comparison of unitary displacements and forces between 2 cardiac myosin isoforms by the optical trap technique: molecular basis for cardiac adaptation. Circ. Res. 82, 1029–1034.
Sugiura, S., Nishimura, S., Yasuda, S., Hosoya, Y., Katoh, K., 2006. Carbon fiber technique for the investigation of single-cell mechanics in intact cardiac myocytes. Nat. Protoc. 1, 1453–1457.
Svrcek, M., Rutherford, S., Chen, A.Y., Provaznik, I., Smaill, B., 2009. Characteristics of motion artifacts in cardiac optical mapping studies. Conf. Proc. IEEE Eng. Med. Biol. Soc. 2009, 3240–3243.
Taggart, P., Lab, M., 2008. Cardiac mechano-electric feedback and electrical restitution in humans. Prog. Biophys. Mol. Biol. 97, 452–460.
Tai, D.C., Caldwell, B.J., LeGrice, I.J., Hooks, D.A., Pullan, A.J., Smaill, B.H., 2004. Correction of motion artifact in transmembrane voltage-sensitive fluorescent dye emission in hearts. Am. J. Physiol. Heart Circ. Physiol. 287, H985–H993.
ter Keurs, H.E., 2012. The interaction of Ca2+ with sarcomeric proteins: role in function and dysfunction of the heart. Am. J. Physiol. Heart Circ. Physiol. 302, H38–H50.
ter Keurs, H.E., Shinozaki, T., Zhang, Y.M., Zhang, M.L., Wakayama, Y., Sugai, Y., Kagaya, Y., Miura, M., Boyden, P.A., Stuyvers, B.D., Landesberg, A., 2008. Sarcomere mechanics in uniform and non-uniform cardiac muscle: a link between pump function and arrhythmias. Prog. Biophys. Mol. Biol. 97, 312–331.
Thompson, S.A., Copeland, C.R., Reich, D.H., Tung, L., 2011. Mechanical coupling between myofibroblasts and cardiomyocytes slows electric conduction in fibrotic cell monolayers. Circulation 123, 2083–2093.
Tomaselli, G.F., Marban, E., 1999. Electrophysiological remodeling in hypertrophy and heart failure. Cardiovasc. Res. 42, 270–283.
Toyoda, T., Baba, H., Akasaka, T., Akiyama, M., Neishi, Y., Tomita, J., Sukmawan, R., Koyama, Y., Watanabe, N., Tamano, S., Shinomura, R., Komuro, I., Yoshida, K., 2004. Assessment of regional myocardial strain by a novel automated tracking system from digital image files. J. Am. Soc. Echocardiogr. 17, 1234–1238.
Trayanova, N.A., Gurev, V., Constantino, J., Hu, Y., 2011. Mathematical models of ventricular mechano-electric coupling and arrhythmia. In: Kohl, P., Sachs, F., Franz, M.R. (Eds.), Cardiac Mechano-electric Coupling and Arrhythmias. Oxford University Press, Oxford; New York, pp. 258–266.
Villarreal, F.J., Waldman, L.K., Lew, W.Y., 1988. Technique for measuring regional two-dimensional finite strains in canine left ventricle. Circ. Res. 62, 711–721.
Wang, K., Terrar, D., Gavaghan, D.J., Mu-u-min, R., Kohl, P., Bollensdorff, C., 2014. Living cardiac tissue slices: An organotypic pseudo two-dimensional model for cardiac biophysics research. Prog. Bio. Mol. Biol. 115 (2-3), 314–327. http://dx.doi.org/10.1016/j.pbiomolbio.2014.08.006.
Wakayama, Y., Miura, M., Stuyvers, B.D., Boyden, P.A., ter Keurs, H.E., 2005. Spatial nonuniformity of excitation-contraction coupling causes arrhythmogenic Ca2+ waves in rat cardiac muscle. Circ. Res. 96, 1266–1273.
Ward, M.L., Williams, I.A., Chu, Y., Cooper, P.J., Ju, Y.K., Allen, D.G., 2008. Stretch-activated channels in the heart: contributions to length-dependence and to cardiomyopathy. Prog. Biophys. Mol. Biol. 97, 232–249.
Westergaard, F., Umapathy, K., Masse, S., Sevapstisidis, E., Asta, J., Farid, T., Nair, K., Krishnan, S., Nanthakumar, K., 2008. Non-linear image registration for correction of motion artifacts during optical imaging of human hearts. In: Conf Proc CCECE/CCGEI, pp. 1729–1732.
White, E., Le Guennec, J.Y., Nigretto, J.M., Gannier, F., Argibay, J.A., Garnier, D., 1993. The effects of increasing cell length on auxotonic contractions; membrane potential and intracellular calcium transients in single guinea-pig ventricular myocytes. Exp. Physiol. 78, 65–78.
Yue Yu, T., Syeda, F., Holmes, A., Osborne, B., Dehghani, H., Brain, K.L., Kirchhof, P., Fabritz, L., 2014. An automated system using spatial oversampling for optical mapping in murine atria. Development and validation with monophasic and transmembrane action potentials. Prog. Bio. Mol. Biol. 115 (2-3), 340–348. http://dx.doi.org/10.1016/j.pbiomolbio.2014.07.012.
Yasuda, S.I., Sugiura, S., Kobayakawa, N., Fujita, H., Yamashita, H., Katoh, K., Saeki, Y., Kaneko, H., Suda, Y., Nagai, R., Sugi, H., 2001. A novel method to study contraction characteristics of a single cardiac myocyte using carbon fibers. Am. J. Physiol. Heart Circ. Physiol. 281, H1442–H1446.
Zabel, M., Koller, B.S., Sachs, F., Franz, M.R., 1996. Stretch-induced voltage changes in the isolated beating heart: importance of the timing of stretch and implications for stretch-activated ion channels. Cardiovasc. Res. 32, 120–130.
Zeng, T., Bett, G.C., Sachs, F., 2000. Stretch-activated whole cell currents in adult rat cardiac myocytes. Am. J. Physiol. Heart Circ. Physiol. 278, H548–H557.
Zhang, Y., Sekar, R.B., McCulloch, A.D., Tung, L., 2008. Cell cultures as models of cardiac mechanoelectric feedback. Prog. Biophys. Mol. Biol. 97, 367–382.

Life Sciences 106 (2014) 40–49

Contents lists available at ScienceDirect

Life Sciences

journal homepage: www.elsevier.com/locate/lifescie

Sustained reduction in blood pressure from electrical activation of the baroreflex is mediated via the central pathway of unmyelinated baroreceptors

Michael J. Turner *, Toru Kawada, Shuji Shimizu, Masaru Sugimachi

Department of Cardiovascular Dynamics, National Cerebral and Cardiovascular Center, Osaka, Japan

ARTICLE INFO

Article history:
Received 13 February 2014
Accepted 17 April 2014
Available online 26 April 2014

Keywords:
Baroreceptor
Baroreflex
Resiniferatoxin
Sympathetic nerve activity

ABSTRACT

Aims: This study aims to identify the contribution of myelinated (A-fiber) and unmyelinated (C-fiber) baroreceptor central pathways to the baroreflex control of sympathetic nerve activity and arterial pressure.
Main methods: Two binary white noise stimulation protocols were used to electrically stimulate the aortic depressor nerve and activate reflex responses from either A-fiber (3 V, 20–100 Hz) or C-fiber (20 V, 0–10 Hz) baroreceptor in anesthetized Sprague-Dawley rats ($n = 10$). Transfer function analysis was performed between stimulation and sympathetic nerve activity (central arc), sympathetic nerve activity and arterial pressure (peripheral arc), and stimulation and arterial pressure (Stim-AP arc).
Key findings: The central arc transfer function from nerve stimulation to splanchnic sympathetic nerve activity displayed derivative characteristics for both stimulation protocols. However, the modeled steady-state gain (0.28 ± 0.04 vs. $4.01 \pm 0.2\%\cdot Hz^{-1}$, $P < 0.001$) and coherence at 0.01 Hz (0.44 ± 0.05 vs. 0.81 ± 0.03, $P < 0.05$) were significantly lower for A-fiber stimulation compared with C-fiber stimulation. The slope of the dynamic gain was higher for A-fiber stimulation (14.82 ± 1.02 vs. 7.21 ± 0.79 dB · decade^{-1}, $P < 0.001$). The steady-state gain of the Stim-AP arc was also significantly lower for A-fiber stimulation compared with C-fiber stimulation (0.23 ± 0.05 vs. 3.05 ± 0.31 mmHg·Hz^{-1}, $P < 0.001$).
Significance: These data indicate that the A-fiber central pathway contributes to high frequency arterial pressure regulation and the C-fiber central pathway provides more sustained changes in sympathetic nerve activity and arterial pressure. A sustained reduction in arterial pressure from electrical stimulation of arterial baroreceptor afferents is likely mediated through the C-fiber central pathway.

Introduction

The arterial baroreflex is an important negative feedback system that regulates arterial pressure (AP) against acute instabilities during daily activities. Any involvement of the arterial baroreflex in the long-term regulation of AP has been discounted because surgical denervation of baroreceptor afferents fails to chronically increase AP (Guyton, 1980; Cowley, 1992). In hypertension, the arterial baroreflex resets to the prevailing AP and loses the ability to suppress sympathetic nerve activity (SNA) and AP effectively (Krieger, 1986). However, experimental animal studies using electrical stimulation (Lohmeier et al., 2012) and baroreceptor unloading (Thrasher, 2005a) have implied that the arterial baroreflex may be able to chronically control AP. Clinical trials using electrical activation of the carotid sinus baroreflex (Baroreflex activation therapy) have recently demonstrated effective long-term lowering of AP in patients with drug-resistant hypertension (Bakris et al., 2012). Although bypassing the baroreceptor transduction property by directly stimulating the baroreceptor afferent fibers may explain the effectiveness of the baroreflex activation therapy, the neural mechanisms involved in the SNA and AP regulations during electrical stimulation of the baroreceptor afferents are still not well understood.

An often-overlooked issue involved in the clinical application of baroreflex activation therapy is the existence of two types of baroreceptor afferents: myelinated axons (A-fiber) and unmyelinated axons (C-fiber). The former constitutes approximately 10–20% and the latter accounts for the remaining 80–90% of the fibers in the aortic depressor nerve (ADN) of the rat (Fazan et al., 2001). While it has long been known that these axon types differ in a number of functional characteristics such as firing rates, threshold pressures, expression of membrane channels, reflex inhibition of SNA, and transfer function characteristics (Brown et al., 1978; Numao et al., 1985; Thoren et al., 1999; Sun et al., 2009), they may also differ in their central processing of dynamic

* Corresponding author at: Department of Cardiovascular Dynamics, National Cerebral and Cardiovascular Center, 5-7-1 Fujishirodai, Suita, Osaka 565-8565, Japan. Tel.: +81 6 6833 5012x2427; fax: +81 6 6835 5403.
E-mail address: michaeljturner@icloud.com (M.J. Turner).

http://dx.doi.org/10.1016/j.lfs.2014.04.016
0024-3205/

input. Previous studies by Kubo et al. (1996) and Petiot et al. (2001) identified the transfer function from ADN stimulation to SNA in rabbits and rats, respectively, but did not deal with differences in fiber type. Furthermore, in studies investigating baroreflex activation therapy, both clinical (Bakris et al., 2012) and animal (Lohmeier et al., 2012), the pulse generator was programmed to target a reduction in AP from hypertensive to control levels. While voltage and frequency guidelines have been used there appears to have been no attempt to actively stimulate either A-fiber or C-fiber baroreceptor afferents and identify their respective contribution to the reduction in AP.

We hypothesized that there is a difference in the dynamic characteristics between A-fiber and C-fiber central pathways, which leads to a difference in the regulation of SNA and AP by each fiber type. Accordingly, the purpose of the present study was to examine the contribution of A- and C-fiber central pathways in the control of SNA and AP by electrically stimulating the left ADN of rats. We devised and utilized dynamic stimulation protocols that preferentially activate A- or C-fiber type baroreceptor afferents.

Materials and methods

Animal preparation

Animal care was provided in strict accordance with the Guiding Principles for the Care and Use of Animals in the Field of Physiological Sciences, approved by the Physiological Society of Japan. All protocols were reviewed and approved by the Animal Subject Committee of the National Cerebral and Cardiovascular Center, Osaka, Japan.

Experiments were completed in 10 male Sprague-Dawley rats (350–450 g). Each rat was anesthetized with an intraperitoneal injection (2 $ml \cdot kg^{-1}$) of a mixture of urethane (250 $mg \cdot ml^{-1}$) and α-chloralose (40 $mg \cdot ml^{-1}$), and mechanically ventilated with oxygen-enriched room air. A venous catheter was inserted into the right femoral vein and 20-fold diluted solution of the above anesthetic mixture was administered to maintain anesthesia (2–3 $ml \cdot kg^{-1} \cdot h^{-1}$). The amount of required anesthesia was determined by testing the withdrawal and blink reflexes and adjusted to maintain AP within a normal range in the absence of ADN stimulation. A heating pad was used to maintain body temperature of the animal at approximately 38 °C. A postganglionic branch of the splanchnic sympathetic nerve was exposed through a left flank incision to record SNA using a pair of stainless steel wire electrodes (Bioflex wire, AS633, Cooner Wire, CA, USA). Silicone glue (Kwik-Sil, World Precision Instruments, FL, USA) was used to secure and insulate the nerve and electrodes (Stocker and Muntzel, 2013). Preamplified nerve signals were band-pass filtered at 150–1000 Hz, and then full-wave rectified and low-pass filtered at a cut-off frequency of 30 Hz using analog circuits to quantify SNA.

Bilateral vagal nerves, carotid sinus nerves and ADNs were sectioned to avoid any confounding effects mediated by native cardiopulmonary and arterial baroreflexes. The sectioned central end of the left ADN was placed on a pair of stainless steel wire stimulating electrodes (Bioflex wire, AS633) and covered with silicone glue (Kwick-Sil). The electrodes were attached to an electrical stimulator (Model SEN-7203, Nihon Kohden, Tokyo, Japan) through a stimulus isolation unit (Model SS-102J, Nihon Kohden).

Stimulation protocols

After surgical procedures were completed, baseline SNA and AP were monitored for 30 min. Two stimulation protocols were employed: step stimulation and dynamic stimulation. The pulse duration of the stimulation was fixed to 0.1 ms. The two stimulation protocols were conducted under control conditions and after a 20-minute perineuronal application of 1 $\mu mol \cdot l^{-1}$ resiniferatoxin (RTX) (LC Laboratories, MA, USA) to the left ADN central to the stimulation site. This dose of RTX can irreversibly block C-fiber conduction without significantly interfering with A-fiber conduction (Reynolds et al., 2006). The sequence of the stimulation protocol was: step – dynamic – dynamic(RTX) – step(RTX).

In the step stimulation protocol ($n = 8$), the left ADN was stimulated for 30 seconds using low-voltage (1–3 V) and high-voltage (18–20 V) settings. These voltages were selected to activate only A-fiber (low voltage) or both A- and C-fibers (high voltage) (Fan and Andresen, 1998; Fan et al., 1999). The high voltage setting is a supramaximal stimulation that is well above the required stimulation intensity to initiate C-fiber baroreceptor action potentials, thus insuring complete recruitment of C-fiber baroreceptors in the ADN. The stimulation frequency was varied among 5, 10, 20, 50 and 100 Hz for each stimulus voltage. The step stimulations were given in random order and 3 minutes apart to allow for full recovery of AP and SNA.

In the dynamic stimulation protocol ($n = 10$), the left ADN was stimulated for 20 minutes. The stimulation frequency was switched between two predefined frequency values every 500 ms according to a computer generated binary white noise sequence. A low-voltage (3 V) and high-frequency (either 20 or 100 Hz) stimulation protocol (LVHf) was used to chiefly estimate dynamic characteristics of the A-fiber baroreceptor central pathway. A high-voltage (20 V) and low-frequency (either 0 or 10 Hz) stimulation protocol (HVLf) was used to chiefly estimate dynamic characteristics of the C-fiber baroreceptor central pathway.

Data analysis

Data were sampled at 200 Hz using a 16-bit analog-to-digital converter. The noise level of SNA was determined by a 10-second average of the SNA signal 2 minutes after intravenous hexamethonium (60 $mg \cdot kg^{-1}$) administration and was defined as zero (Kawada et al., 2010). SNA was normalized by defining the SNA level for 10 seconds preceding the ADN stimulation as 100% activity under control conditions.

In the step stimulation protocol, after applying a 1-second moving average to the data, mean AP (MAP) and SNA responses were quantified as negative changes from the level preceding stimulation (baseline) and designated as ΔMAP and ΔSNA. The negative peak responses and final step responses at 30 seconds were calculated. In the dynamic stimulation protocol, based on 10-Hz resampled data, the transfer function from ADN stimulation to SNA and that from SNA to AP were estimated by using a standard open-loop transfer function analysis described below. The former is referred to as the central arc transfer function and the latter as the peripheral arc transfer function in this paper. The transfer functions from ADN stimulation to AP were also estimated and are referred to as the Stim-AP arc.

Data were analyzed starting from 120 seconds after the initiation of the binary white noise stimulation input. The input–output pairs were resampled at 10 Hz and segmented into 50% overlapping bins of 1024 points each. For each segment, a linear trend was removed, and a Hanning window was applied. Fast Fourier transform was performed to obtain the frequency spectra of the input and output signals. The ensemble averages of the input power spectral density [$S_{XX}(f)$], output power spectral density [$S_{YY}(f)$], and cross spectral density between the input and output signals [$S_{YX}(f)$] were calculated over 12 segments, where f denotes frequency. Finally, the transfer function [$H(f)$] from input to output was estimated as (Bendat and Piersol, 2010):

$$H(f) = \frac{S_{YX}(f)}{S_{XX}(f)} \tag{1}$$

The transfer function is a complex-valued function that can be expressed by the modulus and phase at each frequency. In this study, we refer to the modulus as the dynamic gain. Because the magnitude of SNA varied among animals depending on the recording conditions, two normalization procedures were used. The first normalization procedure, where SNA was normalized by assigning unity to the mean dynamic gain for frequencies below 0.03 Hz, was used for comparison

between transfer functions before and after RTX. The second normalization procedure used the noise level of SNA, recorded after the administration of hexamethonium bromide, as zero and the average SNA during baseline recordings was defined as 100%. The second normalization procedure was used for comparisons between A-fiber and C-fiber related transfer functions.

To quantify the linear dependence between the input and output signals, a magnitude squared coherence function [Coh(f)] was calculated as:

$$\mathrm{Coh}(f) = \frac{|S_{YX}(f)|^2}{S_{XX}(f)S_{YY}(f)} \tag{2}$$

The coherence function is a real-valued function ranging from zero to unity. When the output signal is perfectly explained by linear dynamics with the input signal, the coherence value becomes unity. When the output signal is totally independent of the input signal, the coherence value becomes zero.

Simulation

The central and peripheral arc transfer functions were modeled using mathematical transfer functions according to previous studies To facilitate understanding of SNA and AP regulation via the A-fiber and C-fiber pathways, the central and peripheral transfer functions were modeled. According to previous studies (Kawada et al., 2002, 2010) the central arc transfer functions were modeled as:

$$H_N(f) = K_N \frac{1 + \frac{f}{f_{C1}}j}{\left(1 + \frac{f}{f_{C2}}j\right)^2} \exp(-2\pi\ f\ L_N j) \tag{3}$$

where j represents the imaginary units. K_N is the steady-state gain of the central arc (in $\%\cdot Hz^{-1}$), f_{C1} is the corner frequency determining the derivative characteristics (in Hz), f_{C2} is the corner frequency determining the high-cut characteristics (in Hz), and L_N is the pure dead time (in seconds).

The peripheral arc transfer functions were modeled by a second-order low-pass filter as:

$$H_P(f) = \frac{K_P}{1 + 2\zeta\frac{f}{f_N}j + \left(\frac{f}{f_N}j\right)^2} \exp(-2\pi f L_P j) \tag{4}$$

where K_P is the steady-state gain of the peripheral arc (in $mmHg\cdot\%^{-1}$), f_N is the natural frequency (in Hz), ζ is the damping ratio (unitless), and L_P is the pure dead time (in seconds). To facilitate understanding of the modeled transfer function, step responses were calculated by deriving the system impulse response from the inverse Fourier transform. The step response was then obtained from the time integral of the impulse response (Kawada et al., 2002, 2010). The Stim-AP arc was calculated from a product of the central and peripheral arc transfer functions in the frequency domain. To further aid in understanding of the transfer functions, step responses in the time domain, corresponding to respective model transfer functions were also calculated.

Statistical analysis

All data are presented as mean and standard error. Effects of stimulation frequency and RTX on ΔMAP and ΔSNA in the step stimulation protocol were examined by repeated measures two-way ANOVA. The effect of RTX at each frequency was then examined by paired t-test with Bonferroni correction. Before and after the RTX application, changes in mean SNA and AP levels were examined using repeated measures ANOVA followed by paired t-test with Bonferroni correction for comparisons among conditions of pre-stimulation, LVHf, and HVLf stimulation. The transfer function values (dynamic gain and phase) at 0.01, 0.1 and 1 Hz were also compared using repeated measures ANOVA followed by paired t-test with Bonferroni correction among conditions of LVHf before RTX, LVHf after RTX, HVLf before RTX, and HVLf after RTX. Coherence values were compared using Friedman's test with post-hoc Dunn's multiple comparison test. Differences were considered to be significant at $P < 0.05$ for all statistical analysis.

Results

Low-voltage step stimulation

Representative traces of low-voltage step stimulation at 50 Hz before and after perineuronal application of RTX are shown in Fig. 1a. While stimulation decreased MAP and SNA, the reflex decreases in MAP and SNA returned towards pre-stimulation levels during the 30-second stimulation period. RTX had no significant effect on the SNA and MAP responses. The negative peak responses and the final responses measured at different stimulation frequencies are summarized in Fig. 1b. Low intensity stimulation of the ADN lowered SNA and MAP between 20 and 100 Hz, which was unaffected by the application of RTX.

High-voltage step stimulation

Representative traces of high-voltage step stimulation at 20 Hz before and after perineuronal application of RTX are shown in Fig. 2a. The reflex response in MAP was well sustained during the 30-second stimulation period under the control condition. After the RTX application, the negative peak response and the final response became smaller, and the reduction of MAP was not sustained and returned towards baseline levels. The negative peak responses and the final responses measured at different stimulation frequencies are summarized in Fig. 2b. Large reflex responses in SNA and MAP were observed at 5 Hz and above before RTX application.

Dynamic stimulation

Typical experimental traces during the LVHf and HVLf dynamic stimulation protocols before and after perineuronal application of RTX are shown in Fig. 3. MAP and SNA were not significantly decreased from baseline values by the LVHf stimulation, both before and after the RTX application (Table 1). However, MAP and SNA were significantly decreased from baseline values by the HVLf stimulation before RTX application (MAP: 101 ± 2.7 mmHg compared with 79.4 ± 2.4 mmHg, $P < 0.01$; SNA: 100% compared with 70.4 ± 2.5%, $P < 0.001$). RTX abolished the reduction in MAP and SNA observed during the HVLf stimulation (MAP: 105 ± 3.3 mmHg compared with 99.9 ± 4.4 mmHg, SNA: 116 ± 11% compared with 112.4 ± 8.7%).

Central and peripheral arc transfer functions

The central arc transfer function from ADN stimulation to SNA determined by either LVHf or HVLf stimulation shows that normalized dynamic gain increases as the modulation frequency increases (Fig. 4a). The slope of the dynamic gain and dynamic gain at 1 Hz were significantly smaller for the central arc transfer function estimated by HVLf stimulation (7.21 ± 0.79 $dB\cdot decade^{-1}$, Fig. 4a, right) than those estimated by LVHf stimulation (14.82 ± 1.02 $dB \cdot decade^{-1}$, $P < 0.001$, Fig. 4a, left). The coherence of the transfer function estimated by HVLf was significantly higher compared with LVHf stimulation at 0.01 Hz (0.81 ± 0.03 and 0.44 ± 0.05, $P < 0.05$) and 0.1 Hz (0.77 ± 0.04 and 0.42 ± 0.08, $P < 0.05$). The phase of both transfer functions was close to $-\pi$ radians in the lower frequencies, reflecting the out-of-phase relationship between ADN stimulation and SNA. RTX had little effect on the central arc transfer function estimated by the LVHf stimulation other than an increased dynamic gain at 0.1 Hz (Table 2). However, RTX significantly decreased the dynamic gain of HVLf simulation at modulation frequencies of 0.01 Hz (1.10 ± 0.02 $a.u.\cdot Hz^{-1}$ compared with 0.39 ±

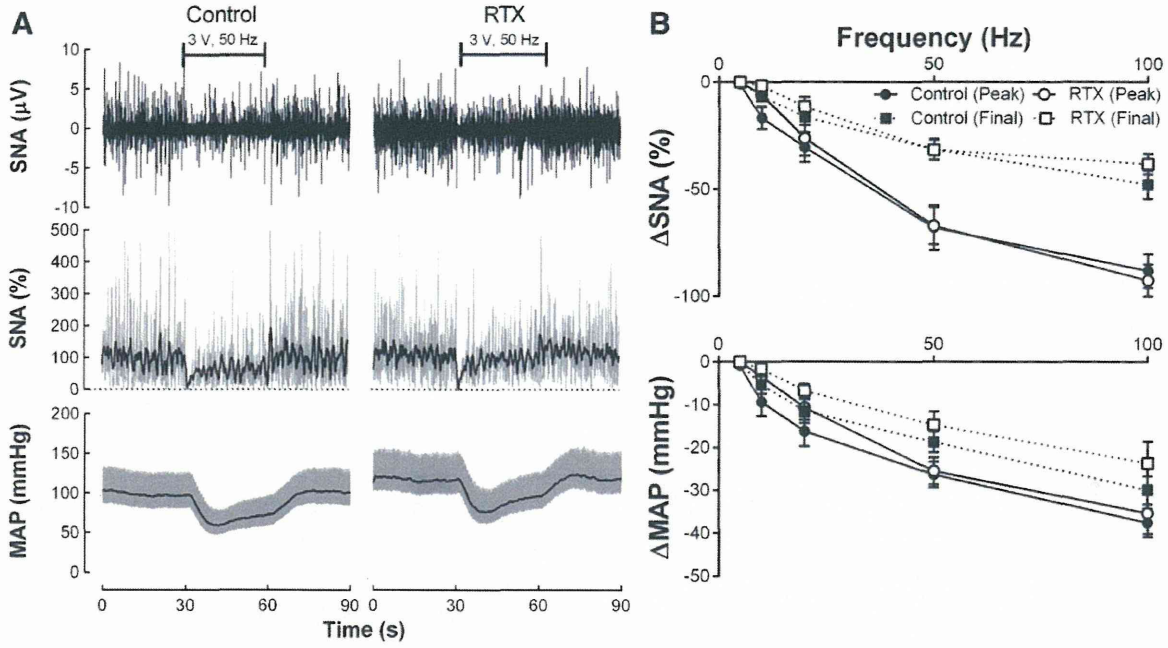

Fig. 1. Sympathetic nerve activity (SNA) and mean arterial pressure (MAP) responses to low voltage (3 V) stimulation. (a) Representative traces showing reflex responses in SNA (top) and MAP (bottom) from electrical stimulation of the ADN at 3 V, 50 Hz. After a transient baroreflex response, SNA and MAP returned towards pre-stimulation levels during the 30-second stimulation period. The gray lines indicate the original 200 Hz signal and the black lines are a 1-second moving average signal. (b) Group data ($n = 8$ in each group) shows high-frequency stimulation of 20 Hz and above was required to evoke notable reflex decreases in SNA (top) and MAP (bottom). At the stimulation frequencies of 20 Hz and above, the magnitude of the final responses (■) in SNA and MAP was approximately 50% and 70–80% of the peak responses (●), respectively. RTX did not significantly affect the negative peak responses (○) or the final responses (□).

0.04 a.u.·Hz^{-1}, $P < 0.01$) and 0.1 Hz (1.27 ± 0.12 a.u.·Hz^{-1} and 0.38 ± 0.04 a.u.·Hz^{-1}, $P < 0.01$) and coherence values at 0.01 Hz (0.81 ± 0.03 and 0.24 ± 0.05, $P < 0.001$), 0.1 Hz (0.77 ± 0.04 and 0.29 ± 0.06, $P < 0.001$) and 1 Hz (0.70 ± 0.04 and 0.33 ± 0.06, $P < 0.05$).

The peripheral transfer function from SNA to AP estimated by either LVHf or HVLf stimulation shows that normalized dynamic gain decreases as the modulation frequency increases (Fig. 4b). The phase of both transfer functions approached zero radians at 0.01 Hz and was delayed by almost -2π radians as the modulation frequency increased to 1 Hz. RTX had no effect on the peripheral arc transfer function estimated by LVHf stimulation (Table 3). RTX significantly decreased the dynamic gain at 0.01 Hz (0.99 ± 0.06 mmHg·a.u.$^{-1}$ and 0.57 ±

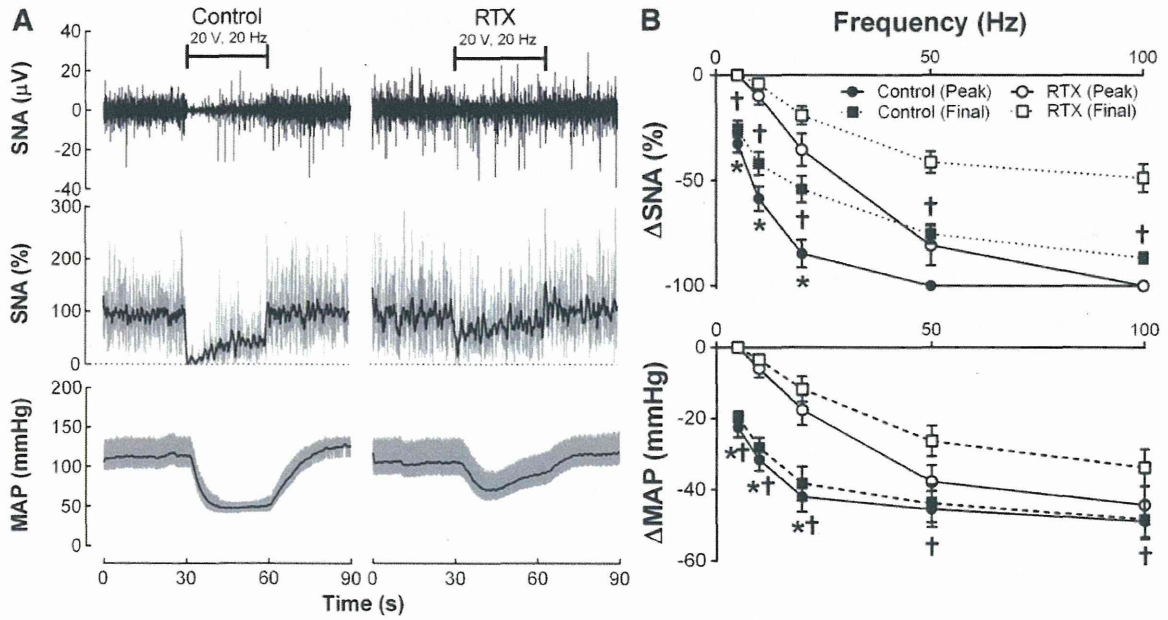

Fig. 2. Sympathetic nerve activity (SNA) and mean arterial pressure (MAP) responses to high voltage (20 V) stimulation. (a) Representative traces showing reflex responses in SNA (top) and MAP (bottom) from electrical stimulation of the ADN at 20 V, 20 Hz. High voltage stimulation resulted in robust responses in SNA and MAP that was sustained throughout the stimulation period. After the application of RTX, responses became brief and returned towards pre-stimulation levels while stimulation was maintained. The gray lines indicate the original 200 Hz signal and the black lines are a 1-second moving average signal. (b) Group data ($n = 8$ in each group) shows that the magnitude of the final responses (■) in SNA and MAP was above 60% and 90% of the peak responses (●), respectively. RTX significantly attenuated the negative peak responses (○) at 5 Hz, 10 Hz, and 20 Hz and the final responses (□) at all frequencies for both SNA and MAP. *$P < 0.01$ for control (peak) vs. RTX (peak); †$P < 0.01$ for control (final) vs. RTX (final).

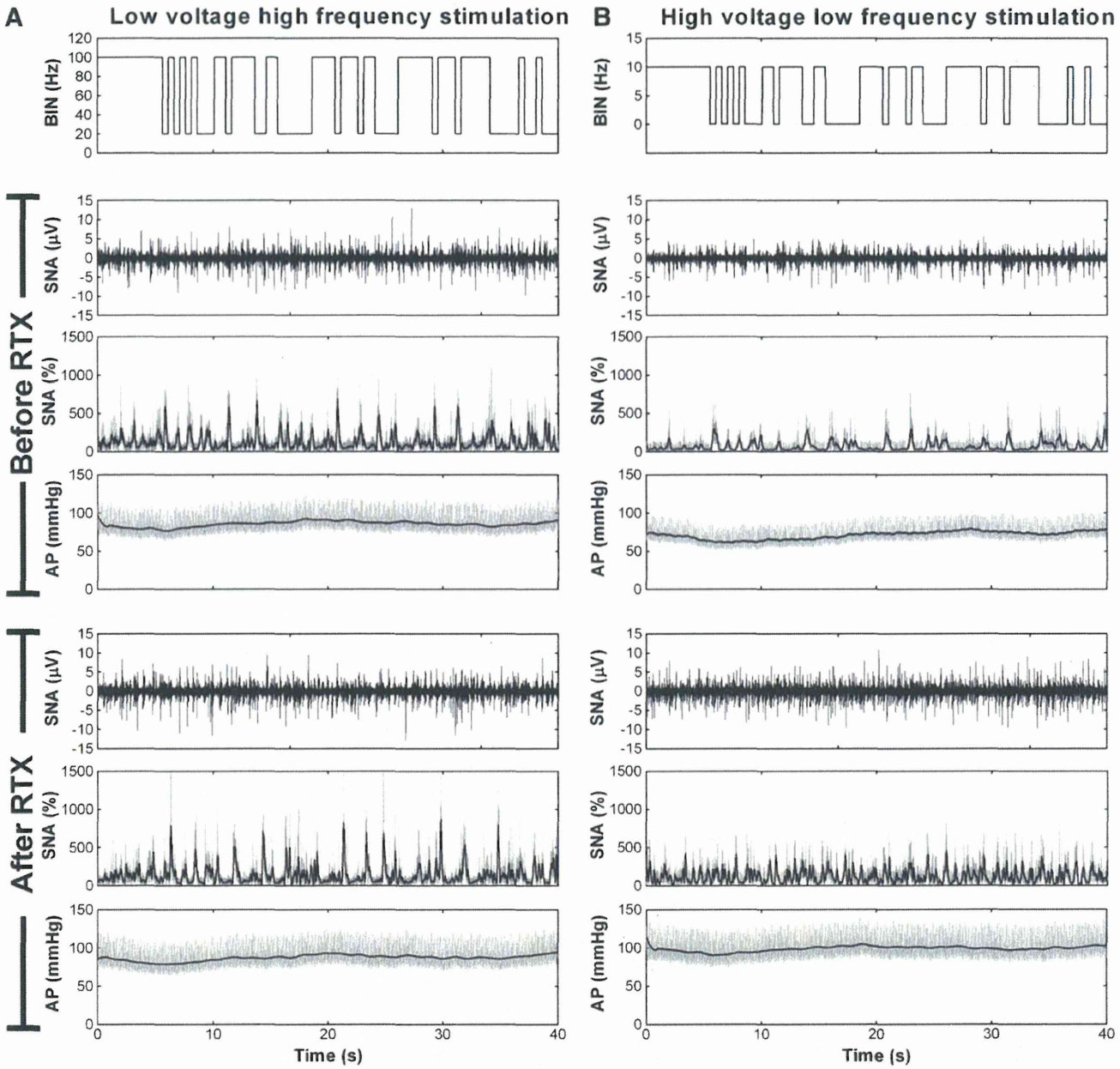

Fig. 3. Typical recordings of binary white noise stimulation (BIN), sympathetic nerve activity (SNA) and arterial pressure (AP) during low voltage (3 V) high frequency stimulation (a) and high voltage (20 V) low frequency stimulation (b). Because of the dynamic nature of the input signal it is not easy to visually identify stimulation-induced reflex responses in SNA and AP. In the SNA plots, the gray lines are the 200 Hz signal, and the black lines indicate 10 Hz resampled data and in the AP plots, the gray lines are the 200 Hz signal and the black line indicates a 1-second moving average.

Table 1
Cardiovascular variables during pre-stimulation conditions and stimulation protocols.

	Before RTX			After RTX		
	Prestim	LVHf	HVLf	Prestim	LVHf	HVLf
SNA, %	100	96.3 ± 11.0	70.4 ± 2.5[a,b]	116 ± 11.0	106 ± 6.9	112 ± 8.7
MAP, mmHg	101 ± 2.7	96.0 ± 5.6	79.4 ± 2.4[c,d]	105 ± 3.3	94.3 ± 4.7	99.9 ± 4.4
HR, bpm	387 ± 6.2	394 ± 10.1	370 ± 9.0	394 ± 6.3	408 ± 10.8	404 ± 4.7

Data are means ± SE ($n = 10$ in each group). SNA, sympathetic nerve activity; MAP, mean arterial pressure; HR, heart rate; Prestim, pre-stimulation conditions; LVHf, low-voltage high-frequency dynamic stimulation; HVLf, high-voltage low-frequency dynamic stimulation; RTX, resiniferatoxin.

[a] $P < 0.001$ vs. Prestim.
[b] $P < 0.001$ vs. LVHf.
[c] $P < 0.01$ vs. Prestim.
[d] $P < 0.05$ vs. LVHf.

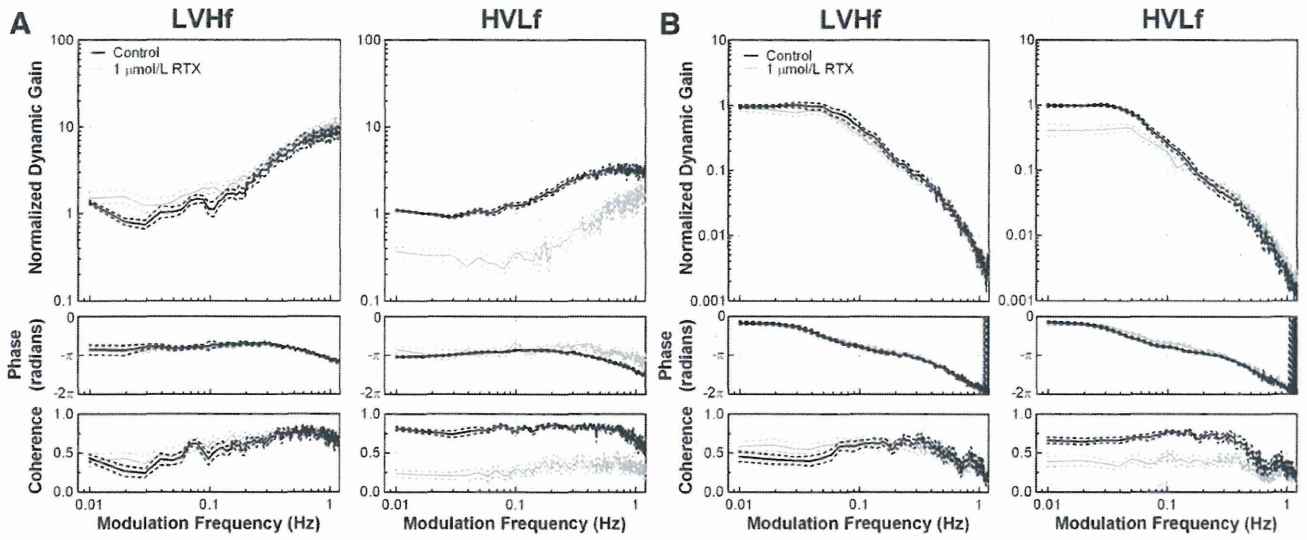

Fig. 4. Effect of RTX on central arc (a) and peripheral arc (b) transfer functions using either LVHf (left) or HVLf (right) stimulation protocols. LVHf, low-voltage high-frequency dynamic stimulation; HVLf, high-voltage low-frequency dynamic stimulation; RTX, resiniferatoxin. In each panel, the solid and dashed lines represent the mean and mean ± SE, respectively.

0.07 mmHg·a.u.$^{-1}$, $P < 0.001$) and coherence values at 0.01 Hz (0.66 ± 0.04 and 0.39 ± 0.07, $P < 0.05$) and 0.1 Hz (0.77 ± 0.02 and 0.46 ± 0.06, $P < 0.001$) of the peripheral arc transfer function estimated by HVLf stimulation.

Stim-AP arc transfer functions

The Stim-AP arc transfer function, estimated by either LVHf or HVLf stimulation, shows that normalized dynamic gain decreases as the modulation frequency increases (Fig. 5). The phase of both transfer functions approached $-\pi$ radians at 0.01 Hz and was delayed by almost -3π radians as the modulation frequency increased to 1 Hz. RTX had no effect on the Stim-AP arc transfer function estimated by LVHf stimulation (Table 4). RTX significantly decreased the dynamic gain at 0.01 Hz (3.05 ± 0.31 mmHg·Hz^{-1} and 0.91 ± 0.10 mmHg·Hz^{-1}, $P < 0.001$) and coherence values at 0.01 Hz (0.70 ± 0.03 and 0.31 ± 0.07, $P < 0.001$) and 0.1 Hz (0.72 ± 0.04 and 0.41 ± 0.07, $P < 0.01$) of the Stim-AP arc transfer function estimated by HVLf stimulation. The gain at 0.01 Hz was also significantly lower for the transfer function estimated by LVHf stimulation compared with HVLf (0.23 ± 0.05 mmHg·Hz^{-1} and 3.05 ± 0.31 mmHg·Hz^{-1}, $P < 0.001$).

Table 2
Transfer function parameters of the baroreflex central arc obtained from LVHf and HVLf stimulation protocols.

Central arc	LVHf	LVHf (RTX)	HVLf	HVLf (RTX)
Gain (a.u.·Hz^{-1})				
0.01 Hz	1.39 ± 0.07	1.69 ± 0.23	1.10 ± 0.02	0.39 ± 0.04[a]
0.1 Hz	1.28 ± 0.2	2.07 ± 0.28[c]	1.27 ± 0.12	0.38 ± 0.04[a]
1 Hz	8.55 ± 1.06	10.28 ± 1.13	3.36 ± 0.23[b]	1.72 ± 0.26
Slope (dB·decade^{-1})				
0.1–1 Hz	14.82 ± 1.02	15.54 ± 1.32	7.21 ± 0.79[b]	15.94 ± 1.64[d]
Phase (radians)				
0.01 Hz	−2.68 ± 0.23	−2.52 ± 0.11	−3.27 ± 0.05	−2.72 ± 0.3
0.1 Hz	−2.74 ± 0.36	−2.51 ± 0.16	−2.72 ± 0.05	−2.54 ± 0.46
1 Hz	−3.36 ± 0.09	−3.31 ± 0.09	−4.24 ± 0.09[b]	−3.18 ± 0.15[d]
Coherence				
0.01 Hz	0.44 ± 0.05	0.40 ± 0.08	0.81 ± 0.03[e]	0.24 ± 0.05[d]
0.1 Hz	0.42 ± 0.08	0.57 ± 0.07	0.77 ± 0.04[e]	0.29 ± 0.06[d]
1 Hz	0.70 ± 0.05	0.73 ± 0.04	0.70 ± 0.04	0.33 ± 0.06[f]

Data are means ± SE ($n = 10$ in each group). LVHf, low-voltage high-frequency dynamic stimulation; HVLf, high-voltage low-frequency dynamic stimulation; RTX, resiniferatoxin.
[a] $P < 0.01$ vs. HVLf.
[b] $P < 0.001$ vs. LVHf.
[c] $P < 0.01$ vs. LVHf.
[d] $P < 0.001$ vs. HVLf.
[e] $P < 0.05$ vs. LVHf.
[f] $P < 0.05$ vs HVLf.

Simulation

Model transfer functions and corresponding step responses are shown in Fig. 6. The parameter values used to simulate the transfer functions were derived from the mean values shown in Table 5. The transfer gain in the lower frequency range (steady-state) was lower in the A-fiber related transfer function than the C-fiber related transfer function in the central arc (0.28 ± 0.04%·Hz^{-1} vs. 4.01 ± 0.2%·Hz^{-1}, $P < 0.001$) and Stim-AP arc (0.15 ± 0.03 mmHg·Hz^{-1} vs. 2.39 ± 0.23 mmHg·Hz^{-1}, $P < 0.001$). There were no significant differences between the A-fiber and C-fiber related transfer functions of the peripheral arc (Table 4). The step responses, corresponding to the respective model transfer functions, provide an intuitive representation of A- and C-fiber related changes in SNA and AP. The peak response was significantly greater (−11.20 ± 0.50% vs. −2.44 ± 0.44%, $P < 0.001$) and time to peak (0.36 ± 0.02 second vs. 0.19 ± 0.01 second, $P < 0.001$) was significantly longer for C-fiber related responses in the central arc step response. There was no significant difference in the peripheral arc step responses.

Discussion

The purpose of this study was to identify the contribution of A- and C-fiber baroreceptor central pathways to the reduction in AP observed during electrical activation of the arterial baroreflex. The present results demonstrate that the C-fiber central pathway contributes more to sustained decreases in SNA and AP than the A-fiber central pathway.

Dynamic characteristics of A- and C-fiber central pathways

Arterial baroreceptors can be classified as either A- or C-fiber type based on the presence of myelin and other distinct characteristics, such as firing rate and threshold pressures. While the differences in firing characteristics of A- and C-fiber baroreceptor afferents are well documented (Thoren et al., 1999), differences in the central processing

Table 3
Transfer function parameters of the baroreflex peripheral arc obtained from LVHf and HVLf stimulation protocols.

Peripheral arc	LVHf	LVHf(RTX)	HVLf	HVLf(RTX)
Gain (mmHg·a.u.$^{-1}$)				
0.01 Hz	0.97 ± 0.06	0.98 ± 0.01	0.99 ± 0.06	0.57 ± 0.07[a]
0.1 Hz	0.52 ± 0.08	0.38 ± 0.03	0.29 ± 0.03[b]	0.21 ± 0.02
1 Hz	0.007 ± 0.001	0.007 ± 0.001	0.003 ± 0.001[c]	0.005 ± 0.001
Slope (dB·decade^{-1})				
0.1–1 Hz	−32.6 ± 0.94	−29.3 ± 2.17	−34.3 ± 1.05	−26 ± 1.72[a]
Phase (radians)				
0.01 Hz	−0.56 ± 0.11	−0.53 ± 0.06	−0.44 ± 0.07	−0.66 ± 0.17
0.1 Hz	−2.41 ± 0.12	−2.33 ± 0.12	−2.44 ± 0.08	−2.11 ± 0.14[d]
1 Hz	−4.98 ± 0.29	−5.01 ± 0.29	−5.18 ± 0.19	−5.27 ± 0.13
Coherence				
0.01 Hz	0.45 ± 0.06	0.59 ± 0.06	0.66 ± 0.04	0.39 ± 0.07[d]
0.1 Hz	0.60 ± 0.06	0.67 ± 0.04	0.77 ± 0.02[c]	0.46 ± 0.06[a]
1 Hz	0.36 ± 0.07	0.33 ± 0.06	0.32 ± 0.06	0.30 ± 0.05

Data are means ± SE (n = 10 in each group). LVHf, low-voltage high-frequency dynamic stimulation; HVLf, high-voltage low-frequency dynamic stimulation; RTX, resiniferatoxin.
[a] $P < 0.001$ vs. HVLf.
[b] $P < 0.01$ vs. LVHf.
[c] $P < 0.05$ vs LVHf.
[d] $P < 0.05$ vs. HVLf.

between A-fiber and C-fiber central pathways remain to be fully elucidated. The present study demonstrated that LVHf dynamic stimulation, which predominantly activates the A-fiber baroreceptor afferents, produced a central arc transfer function with strong derivative characteristics (Fig. 4a, left). This may indicate that the A-fiber central pathway primarily contributes to the SNA regulation in the higher frequency range. In contrast, HVLf dynamic stimulation, which predominantly activates the C-fiber baroreceptor afferents, produced a central arc transfer function with less derivative characteristics before the RTX application (Fig. 4a, right). Therefore, the C-fiber central pathway contributes to the SNA regulation both in the lower frequency range and in the higher frequency range. These characteristics conform to known characteristics of A- and C-fiber baroreceptor firing (Thoren et al., 1999).

The dynamic gain of the C-fiber related central arc transfer function was over an order of magnitude higher than that of the A-fiber related central arc transfer function (Fig. 6a). These data indicate that, per unit stimulation frequency, C-fiber baroreceptor activity results in a significantly greater reduction in SNA than A-fiber baroreceptor activity. At the same time, it is important to remember normal physiological firing rates of A-fiber (10–100 Hz) and C-fiber (0–20 Hz) baroreceptor axons (Thoren et al., 1999). Even after we take this difference into account it seems that the C-fiber central pathway contributes more to the SNA regulation in the lower frequency range compared with the A-fiber central pathway. The simulation of the Stim-AP arc (Fig. 6c) also indicates that the contribution of the C-fiber pathway is greater in the regulation of AP than that of A-fiber pathway because the peripheral arc transfer function did not differ significantly between A- and C-fiber related transfer functions (Fig. 6b).

To further interpret how each baroreceptor subtype contributes to the control of SNA it is important to take coherence into account.

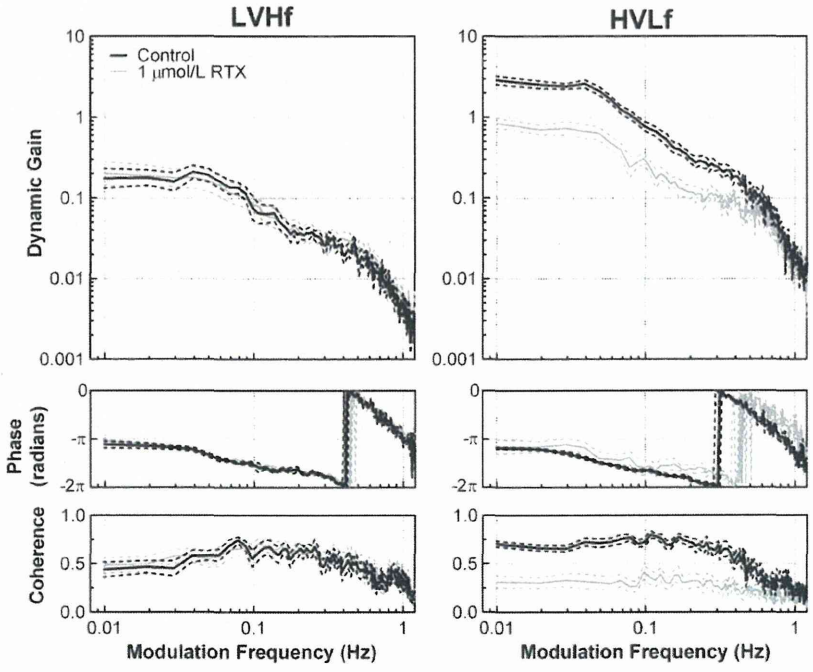

Fig. 5. Effect of RTX on Stim-AP arc transfer functions using either LVHf (left) or HVLf (right) stimulation protocols. LVHf, low-voltage high-frequency dynamic stimulation; HVLf, high-voltage low-frequency dynamic stimulation; RTX, resiniferatoxin. In each panel, the solid and dashed lines represent the mean and mean ± SE, respectively.

Table 4
Transfer function parameters of the Stim-AP arc obtained from LVHf and HVLf stimulation protocols.

Stim-AP Arc	LVHf	LVHf (RTX)	HVLf	HVLf (RTX)
Gain (mmHg·Hz^{-1})				
0.01 Hz	0.23 ± 0.05	0.29 ± 0.06	3.05 ± 0.31[b]	0.91 ± 0.10[a]
0.1 Hz	0.10 ± 0.02	0.10 ± 0.02	0.83 ± 0.10[b]	0.35 ± 0.06[a]
1 Hz	0.006 ± 0.001	0.008 ± 0.002	0.026 ± 0.004[b]	0.024 ± 0.003
Slope (dB·decade^{-1})				
0.1–1 Hz	−18.6 ± 1.40	−16.5 ± 1.34	−23.4 ± 0.87[e]	−15.6 ± 1.07[a]
Phase (radians)				
0.01 Hz	−3.50 ± 0.22	−3.25 ± 0.11	−3.73 ± 0.06	−3.12 ± 0.46
0.1 Hz	−4.73 ± 0.16	−4.78 ± 0.13	−5.19 ± 0.07	−4.43 ± 0.46
1 Hz	−5.95 ± 0.15	−5.61 ± 0.10	−6.80 ± 0.13[d]	−5.90 ± 0.21[c]
Coherence				
0.01 Hz	0.44 ± 0.08	0.48 ± 0.08	0.70 ± 0.03	0.31 ± 0.06[a]
0.1 Hz	0.55 ± 0.08	0.65 ± 0.05	0.72 ± 0.04	0.41 ± 0.07[a]
1 Hz	0.32 ± 0.05	0.38 ± 0.05	0.25 ± 0.04	0.19 ± 0.03

Data are means ± SE (n = 10 in each group). LVHf, low-voltage high-frequency dynamic stimulation; HVLf, high-voltage low-frequency dynamic stimulation; RTX, resiniferatoxin.
[a] $P < 0.001$ vs. HVLf.
[b] $P < 0.001$ vs. LVHf.
[c] $P < 0.01$ vs. HVLf.
[d] $P < 0.01$ vs. LVHf.
[e] $P < 0.05$ vs. LVHf.

Table 5
Model parameters and step response.

	A-fiber related	C-fiber related
Central arc		
K_N, %·Hz^{-1}	0.278 ± 0.042	4.014 ± 0.2[a]
f_{C1}, Hz	0.093 ± 0.015	0.133 ± 0.01[b]
f_{C2}, Hz	1.85 ± 0.15	0.92 ± 0.08[a]
L_N, s	0.11 ± 0.003	0.155 ± 0.008[a]
Peak response, %	−2.44 ± 0.44	−11.2 ± 0.5[a]
Time to peak, s	0.19 ± 0.01	0.36 ± 0.02[a]
Peripheral arc		
K_P, mm·%$^{-1}$	0.52 ± 0.07	0.60 ± 0.06
f_{NP}, Hz	0.06 ± 0.01	0.07 ± 0.01
ζ	1.00 ± 0.07	1.06 ± 0.09
L_P, s	0.44 ± 0.02	0.45 ± 0.01
Steady state response, mmHg	0.51 ± 0.06	0.58 ± 0.05
Initial slope, mmHg·%$^{-1}$·s^{-1}	0.049 ± 0.007	0.058 ± 0.005

Data are means ± SE (n = 10 in each group).
[a] $P < 0.001$.
[b] $P < 0.05$.

Estimates of coherence vary between zero and unity. Coherence equal to unity implies perfect linear coupling between input and output signals, whereas a coherence of zero indicates an output that is linearly independent from the input (Bendat and Piersol, 2010). Coherence is lowered by noise components in the output signal unrelated to the input stimulation and nonlinear system responses. The coherence of the A-fiber related central arc transfer function was low between 0.01 and 0.1 Hz, which suggests that the A-fiber central pathway did not contribute much to the SNA variation in these low modulation frequencies. In contrast, the coherence of the C-fiber related central arc transfer function was relatively high at all modulation frequencies, which indicates that the C-fiber central pathway governed the SNA output in the frequency range under study.

A possible mechanism for the observed difference in A- and C-fiber central pathways is neuronal adaptation. Adaptation is generally defined as a decline in response during a maintained stimulus of constant intensity. Adaptation of baroreceptor activity from a sustained elevation in input pressure is dependent on a K^+ current that is blocked by 4-aminopyridine (Chapleau et al., 1993). Baroreceptive second order neurons may also adapt to sustained baroreceptor input in a similar way to the baroreceptor afferents that they are associated with. The C-fiber central pathway may not adapt to the same degree as the A-fiber central

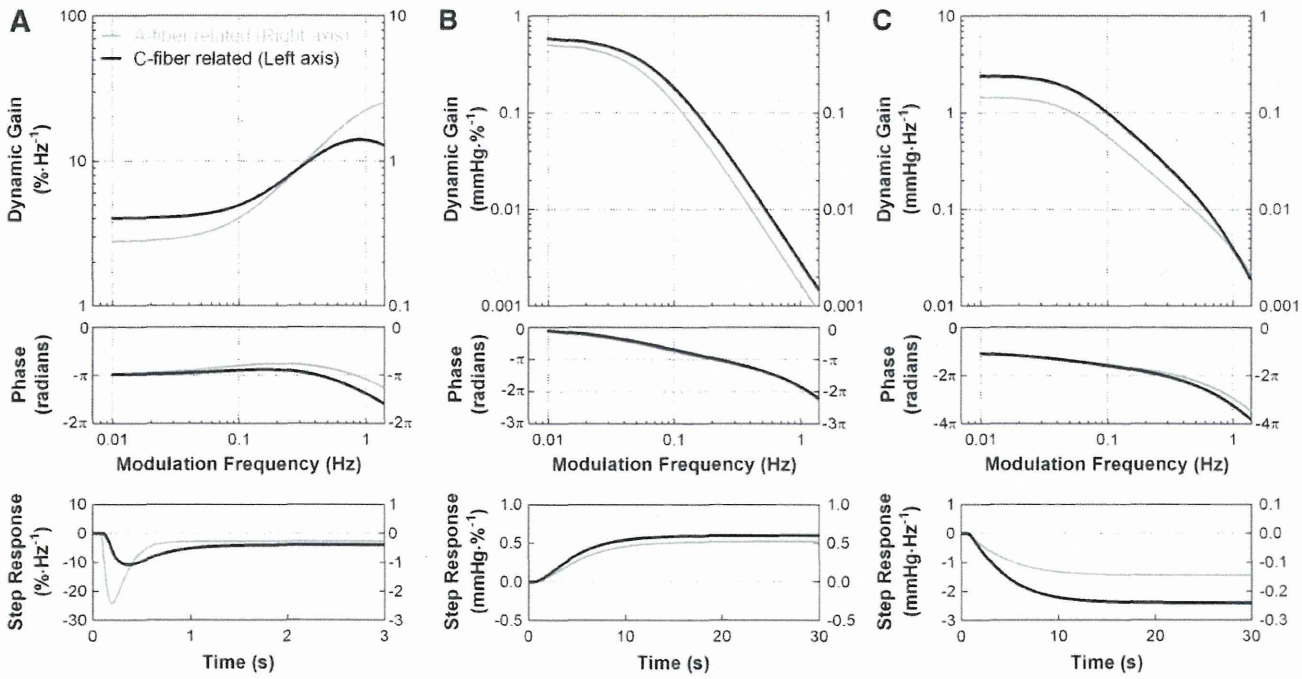

Fig. 6. Simulation of transfer functions and step responses of the central arc (a), peripheral arc (b), and Stim-AP arc (c). In the central arc (a) and Stim-AP arc (c) transfer functions, dynamic gain is displayed in units of output change per stimulation frequency. The ordinate (right axis) for A-fiber related transfer functions (gray lines) in the central arc (a) and Stim-AP arc (c) was shifted upwards by an order of magnitude for relative comparison with C-fiber related transfer functions (black lines). A- and C-fiber related transfer functions and step responses of the Stim-AP arc are the product of the central and peripheral arcs. The majority of the difference in the transfer functions and step responses between A- and C-fiber related responses of the total baroreflex can be attributed to differences in the central arc.